Water-Mediated Charge Transfer and Electron Localization in a Co₃Fe₂ Cyanide-Bridged Trigonal Bipyramidal Complex

Emily Hruska¹, Quansong Zhu¹, Somnath Biswas¹, Matthew T. Fortunato¹, Dustin R. Broderick¹, Christine M. Morales², John M. Herbert¹, Claudia Turro¹, and L. Robert Baker^{1*}

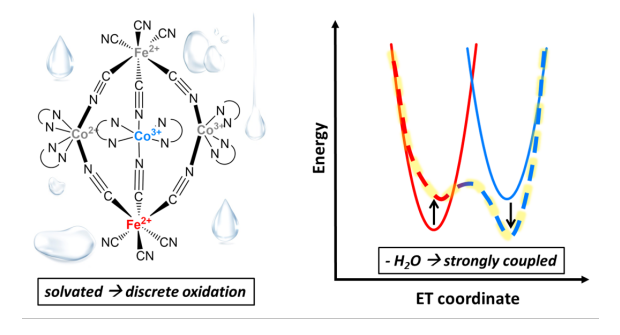
¹Department of Chemistry and Biochemistry, The Ohio State University, Columbus, OH 43210

²Department of Chemistry, University of Mount Union, Alliance, OH 44601

Received October 15, 2023; E-mail: baker.2364@osu.edu

Abstract: The effects of temperature and chemical environment on a pentanuclear cyanide-bridged, trigonal bipyramidal molecular magnet has been investigated. Using element and oxidation state specific near-ambient pressure XPS (NAP-XPS) to probe charge transfer and second order, nonlinear vibrational spectroscopy, which is sensitive to symmetry changes based on charge (de)localization coupled with DFT a detailed picture of environmental effects on charge-transfer induced spin transitions is presented. The molecular cluster, $Co_3Fe_2(tmphen)_6(\mu-CN)_6(t-CN)_6$, abbrev. Co_3Fe_2 , shows changes in electronic behavior depending on chemical environment. NAP-XPS shows that temperature changes induce a metal-to-metal charge transfer (MMCT) in Co₃Fe₂ between a Co and Fe center, while cycling between ultrahigh vacuum and 2 mbar water at constant temperature, causes oxidation state changes not fully captured by the MMCT picture. Sum frequency generation vibrational spectroscopy (SFG-VS) probes the role of the cyanide ligand, which controls the electron (de)localization via the superexchange coupling. Spectral shifts and intensity changes indicate a change from a charge delocalized, Robin-Day Class II/III high spin state to a charge localized, Class I low spin state consistent with DFT. In the presence of a H-bonding solvent the complex adopts a localized electronic structure, while removal of the solvent delocalizes the charges and drives a MMCT. This change in Robin-Day classification of the complex as a function of chemical environment results in reversible switching of the dipole moment, analogous to molecular multiferroics. These results illustrate the important role of chemical environment and solvation on underlying charge and spin transitions in this and related complexes.

TOC Graphic



Introduction

Understanding the nature of spin dynamics in molecules is

critical for realizing the potential applications of molecular switches, which range from molecular design of information storage systems 1 to quantum information processing $^{2-4}$ and quantum sensing 1,5 to photochemistry 6,7 and photocatalysis. 8,9 Each of these applications can benefit from the ability to control the local charge and spin configurations in multimetallic systems. In both solid state systems as well as molecular complexes, this capability is often derived from bistability, which enables switching between various stable or metastable charge and spin configurations based on external stimuli.

For example, the discovery of Prussian blue (PB) analogues and their extended magnetic ordering at elevated temperatures has led to a high interest in understanding cyanide chemistry for magnetic applications. ^{10–14} Translating the PB ground work to molecular complexes of varied geometries has paved the way for studies in many interesting mechanistic behaviors, including single molecule magnetism, ¹⁵ cyanide linkage isomerism, ^{16,17} charge transfer induced spin transitions (CTIST), ^{18–23} and light induced excited spin state trapping (LIESST). ^{24–26}

Synthetic protocols for the design of multimetallic complexes has enabled a range of structural motifs to be studied in the search for bistable molecular magnets. While examples exist of organic- $^{27-30}$ and lanthanide-based molecular magnets, $^{31-36}$ low-cost, earth-abundant transition metal complexes represent an attractive and widely-studied platform for designing molecular bistability based on electron spin. $^{35,37-41}$

Bimetallic systems consisting of $\rm d^4$ through $\rm d^7$ transition metals often display spin transitions that are coupled with electron exchange between metal centers. Such spin crossover events may be triggered by various external stimuli, including temperature, light, or chemical environment; however, achieving molecular bistability at room temperature remains a challenge. A number of recent studies have shown that high nuclearity clusters with intentional ligand motifs can provide bistable spin configurations with high ground state magnetic susceptibility. $^{36,42-44}$

While synthetic tunability of the ligand framework enables preparation of a variety of model complexes, a lack of direct measurements of element specific oxidation state and charge (de)localization limits current mechanistic understanding that could otherwise inform rational design of functional molecular systems. The Robin-Day classification system categorizes mixed valence systems by the strength of the electronic coupling between metal centers. ^{45–47} In multimetallic complexes based on cyanide bridging ligands, the strength of superexchange coupling ultimately defines the degree of localization of valence electrons in the system. In this study, we focus on a pentanuclear clus-

ter $\text{Co}_3\text{Fe}_2(\text{tmphen})_6(\mu\text{-CN})_6(t\text{-CN})_6$ (tmphen = 3,4,7,8-tetramethyl-1,10-phenanthroline) with bridging and terminal cyanide ligands, $\mu\text{-CN}$ and t-CN, respectively, abbreviated Co_3Fe_2 .

This complex has been reported to display electronic and magnetic bistability, which can be switched using both temperature and visible light. 18,48,49 However, it has also been reported that both the optical properties and magnetic susceptibility are sensitive to chemical environment, where exposure to moisture induces a color change as well as a significant reduction in the magnetic susceptibility at a fixed temperature. 48,49 Using a combination of near-ambient pressure X-ray photoelectron spectroscopy (NAP-XPS), Raman spectroscopy, sum frequency generation vibrational spectroscopy (SFG-VS), and DFT calculations, we investigate the effect of chemical environment on the local oxidation states of both Co and Fe centers as well as the degree of electron (de)localization based on the effect of solvation on the superexchange coupling in this complex. We determine that the classification of the complex plays an important role in the mechanism for electronic and magnetic bistability. We also show that switching between a Class I and a Class II/III system involves large changes in the dipole moment of the molecule, extending the properties that can be reversibly switched in this bistable system. This work highlights the critical role of molecular solvation on the electronic and magnetic properties of this and related systems and shows that mechanistic understanding of external switching depends strongly on the strength of electronic superexchange, which varies significantly as a function of chemical environment.

Experimental Synthesis

The synthetic protocol of the Co₃Fe₂ complex has been previously investigated and reported by Dunbar et al. ^{17,48,49} and is detailed in the Supporting Information. In short, a hydrous cobalt nitrate was dissolved in acetonitrile and treated with the coordinating ligand, tetramethyl-1,10-phenanthroline. The iron salt dissolved in acetonitrile was slowly added to the solution. After filtration and 2 days wait time, the anhydrous crystal was collected. Filtration in a humid atmosphere produced the blue solid form, which was used for all further experiments. Extensive characterization of the complex after synthesis is provided in the Supporting Information.

Sample Preparation

Spectroscopic samples were prepared by drop-casting a saturated solution of the blue solid phase on ozone cleaned Au substrates. The Au substrates were prepared by depositing a Au thin film layer on Si or CaF₂ substrate using electron beam evaporation (Denton DV-502A E-Gun Evaporator). They were further cleaned in an ozone cleaner for 30 minutes to remove any potential contaminants on the surface before drop-casting the Co₃Fe₂ solution. SFG samples had a measured volume of 10 $\mu \rm L$ drop-casted on the substrate to produce consistent signal intensity, while the shallow probe depth of XPS measurements allowed for a thicker layer to give reproducible results.

X-ray Photoemission Spectroscopy (XPS)

High resolution XPS analysis was performed using a Kratos Axis Ultra X-ray photoelectron spectrometer with a monochromatic Al K α X-ray source and a photon energy of 1486.6 eV. Using the Casa XPS software, Fe 2p, Co 2p,

and C 1s windows were fit with a Shirley background and a Gaussian-Lorentzian line shape of 70:30 ratio. All spectra were calibrated to the adventitious C feature at 284.5 eV. Further details of the parameters used for the fitting are included in the Supporting Information section 2.

Near-Ambient Pressure X-ray Photoemission Spectroscopy (NAP-XPS)

NAP-XPS was performed using the SPECS NAP-XPS system in the Surface Analysis Facility at Ohio State University. The system is equipped with a NAP-reaction cell where 0.5 and 2 mbar of a given solvent in the gas phase was introduced via a vial on the instrument manifold following freeze pump cycles to purify. Temperature-dependent experiments were performed at sweeping points between 150-375 K in vacuum conditions.

Raman Microscopy

Raman spectra were acquired using a Renishaw InVia Microscope. The excitation wavelength is 785 nm. The sample is held in the same cell used in the SFG measurements. The beam is focused on the front side of the sample using a Nikon $(10\mathrm{x}/0.30~\mathrm{NA}, 17.5\mathrm{mm}$ working distance) objective and has a diameter of 2 $\mu\mathrm{m}$. The power of the excitation beam at the sample is about 50 mW. During the measurement, direct Ar flow or water vapor flow purged by Ar was introduced into the cell, and the corresponding Raman spectra were collected three times with 60 s integration time for each. Three spectra were averaged and the background spectrum obtained from bare Au in each condition were subtracted to obtain the final spectra.

Vibrational Sum Frequency Generation (SFG) spectroscopy

SFG spectra were measured through a homemade cell using the frontside geometry. The laser instrument setup has been described previously. 50,51 In short, the Ti:Sapphire regenerative amplifier (Spectra Physics-Solstice) outputs 90 fs pulses at 800 nm with a repetition rate of 2 kHz. 70% of the output is used to pump an optical parametric amplifier (Topas Prime), which generates the IR beam with a tunable wavelength and a spot size of 0.032 mm². The remaining 30% visible beam is spectrally narrowed to about 10 cm⁻¹ using an air-gap etalon (TecOptics), and focused to a spot size of 0.128 mm². The incident angle for beams at the sample is 47° . The IR beam is centered at about 2100 ${\rm cm}^{-1}$ and has an energy of 3 $\mu {\rm J}$, while the visible beam has an energy of 10 μ J. Each spectrum was collected by delaying the visible beam relative to the IR beam by about 850 fs (Supporting Information), with an integration time of 2 minutes. To mirror the isolated vacuum chamber system of the NAP-XPS measurements, the beams go through a CaF₂ window and a gas gap before they reach the drop-cast Co₃Fe₂ sample on the Au substrate, where sum frequency signal is generated in an isolated homemade cell. A continuous Ar (> 99.998%, Praxair) gas flow purging through the cell at a rate of 616 sccm was maintained throughout the measurement for vacuum-like conditions. For measurements in solvated chemical environments, the Ar gas flow went through a gas-tight vial first, which contained ultrapure water or methanol, and carried the evaporated chemicals into the cell.

Electronic Structure Calculations

Density functional theory (DFT) calculations were performed starting from the crystal structure in Ref. 49, which was then relaxed at the B(35)LYP+D3/def2-SV(P) level.

The exchange-correlation (xc) functional,

$$E_{\rm xc}^{\rm B(35)LYP} = 0.65 E_{\rm x}^{\rm B88} + 0.35 E_{\rm x}^{\rm HF} + E_{\rm c}^{\rm LYP}$$

is one that is recommended for systems at the Class II/III borderline, 47,52 combined with an empirical dispersion correction. 53 These calculations were performed using a broken-symmetry DFT approach 54 and are intended to elucidate energy differences between various spin and oxidation states. All calculations were performed using Q-Chem v. 6.1. 55

Results and Discussion

Figure 1A shows the nominal process for electron transfer in a Co₃Fe₂ system assuming Robin-Day Class I, ⁴⁷ where the system has weak coupling between metal centers. In this picture, electron transfer is characterized by electron localization to discrete metal centers, such that each metal exists in a well-defined oxidation state. This case is depicted in Figure 1A, where charge transfer occurs between an Fe center and a single Co center (shown in blue), with two Co centers acting as spectators (shown in grey). Alternatively, Figure 1B shows the analogous process for the case where the Co₃Fe₂ complex is categorized as a Class II/III system, with a small barrier for interconversion. Systems in Class $\rm II/III$ may exhibit solvent- or conformation-driven switching between localized oxidation states. 46 Assuming strong coupling of the axial Fe centers to each of the equatorial Co centers through the bridging cyano ligands, as suggested by electronic structure calculations that are described below, electronic superexchange allows delocalization of electrons across multiple metal centers. In this scenario, it may become difficult to identify a single Co center involved in the charge transfer as electronic exchange between Fe and its three nearest neighbor Co centers becomes facile. This is depicted in Figure 1B as participation of all three equatorial Co centers (shown in blue) in the charge transfer event, making for a fully delocalized Class II/III system with respect

to the Co sites.

A measurement that samples the system at a time scale slower than the electronic exchange rate will observe an average oxidation state based on electron sharing between nearly equivalent Co centers rather than three distinct sites. As such, the distinction between Class II, Class II/III, and Class III may depend on the time scale of the spectroscopic technique that is used, ⁴⁷ and Class II/III systems may exhibit characteristics of both localized and delocalized valence electrons. 46 Additionally, the molecular symmetry increases and the dipole moment in the equatorial plane becomes negligible because of the strong coupling of the Co centers across the bridging cyanide ligands. In either case 1A or 1B, a metal-to-metal charge transfer (MMCT) event can be triggered depending on the environment of the molecule (temperature, solvent, etc.). However, given the two possibilities for charge dynamics, it becomes necessary to probe the metal centers locally to gain a better understanding of the nature of the charge transfer and associated spin transition based on the strength of electronic coupling in the system.

Electronic Structure Calculations

Broken-symmetry DFT calculations were used to investigate model spin/oxidation states. These calculations start from an initial guess having integer oxidation states on each metal site, from which we attempt to find an orbital-optimized solution of the Kohn-Sham equations that resembles the initial guess. (This procedure has sometimes been called the "generalized ionic fragment" approach. ⁵⁶) The broken-symmetry solution is necessarily spin-contaminated but such calculations can provide information regarding whether intervalence charge transfer, and thus charge delocalization, is energetically feasible. To do so, one needs to examine spin densities on the metal sites for various broken-symmetry solutions.

Figure 2A shows the spin density at the DFT-optimized geometry of a low-spin (S=3/2) state with the configura-

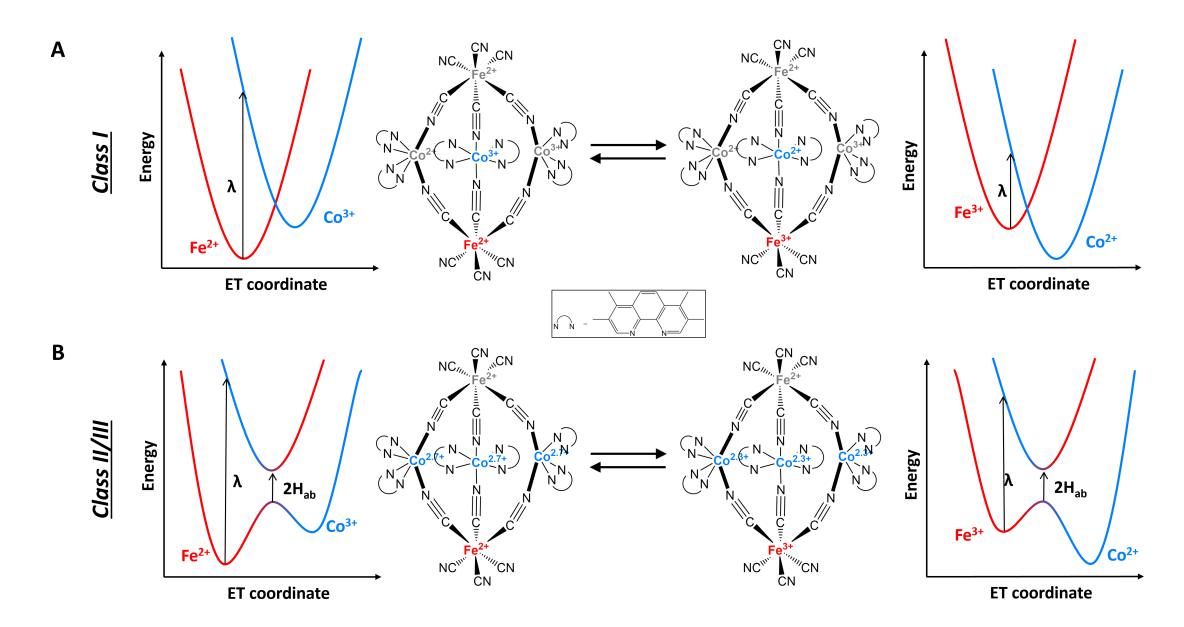


Figure 1. (A) Co_3Fe_2 (middle) with one Fe (red) and one Co (blue) involved in a reversible MMCT. The electron transfer versus energy plots to the left and right of each structure depict the stabilization of an electron on either Fe or Co centers under the Class I localized charge picture. (B) Co_3Fe_2 (middle) with one Fe (red) and three Co (blue) involved in a reversible MMCT. The electron transfer versus energy plots to the left and right of each structure depict the shared delocalization of an electron on Fe and Co centers under the Class II/III delocalized charge picture.

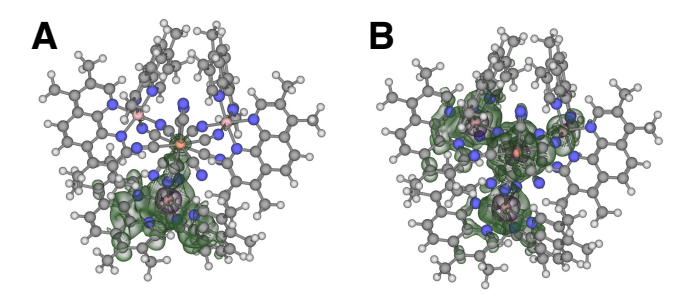


Figure 2. Spin densities $(\rho_{\alpha} - \rho_{\beta})$ for Co_3Fe_2 in (A) the $(\text{Co}^{2+})(\text{Co}^{3+})_2(\text{Fe}^{2+})_2$ state with S=3/2 and (B) the $(\text{Co}^{2+})_2(\text{Co}^{3+})(\text{Fe}^{2+})(\text{Fe}^{3+})$ state with S=7/2. The geometry in both cases is that optimized geometry for the S=3/2 state. Both isosurfaces contain 90% of the spin density and are plotted looking down the Fe–Fe axis at the center. The Co_1 site, which maintains high-spin Co(II) character, is located at the bottom.

tion $(\mathrm{Co}^{2+})(\mathrm{Co}^{3+})_2(\mathrm{Fe}^{2+})_2$, consisting of a single $\mathrm{Co}(\mathrm{II})$ ion in a high-spin configuration and low-spin configurations on the remaining metal centers. Crystallographic data demonstrate that the temperature-dependent magnetic properties of Co₃Fe₂ are associated with changes in oxidation state at the Co₂ and Co₃ sites, whereas Co₁ (located at the bottom in Figure 2) remains high-spin Co(II). 18,49 In accord with the crystal structure that was used as a starting point, we obtain Co-N bond lengths that are ~ 0.2 Å longer at the Co_1 site as compared to Co_2 or Co_3 , characteristic of a Class II or Class II/III system. ^{45,47} Despite concerns that vacuum-exposed anionic moieties (such as CN⁻) can cause DFT convergence problems, ^{57,58} or that vacuum boundary conditions exaggerate charge delocalization (tending toward Class III), ⁴⁷ we obtain similar geometries when using a polarizable continuum model ^{59,60} to add low-dielectric boundary conditions.

Figure 2B shows the spin density for a higher-spin S=7/2 configuration, representing $(\mathrm{Co^{2+}})_2(\mathrm{Co^{3+}})(\mathrm{Fe^{2+}})(\mathrm{Fe^{3+}})$, obtained at the geometry that was optimized for the S=3/2 state. The configuration in Figure 2B represents a model in which $\mathrm{Co_1}$ and $\mathrm{Co_2}$ are both high-spin $\mathrm{Co(II)}$ while one of the Fe atoms has been oxidized to Fe(III) in order to maintain charge neutrality. According to calculations at the B(35)LYP+D3/def2-SV(P) level, the S=7/2 configuration is 7 kcal/mol higher in energy than the S=3/2 configuration, at the geometry of the latter, although this energy difference is sensitive to the fraction of exact exchange and we regard this 7 kcal/mol difference as immaterial. Spin contamination in these calculations is not severe: $\langle \hat{S}^2 \rangle = 3.76$ and 16.01 a.u. for the low- and high-spin states, vs. spin-pure theoretical values of 3.75 and 15.75.

We conclude that broken-symmetry DFT calculations are consistent with both states having nearly the same energy. These calculations say nothing about the barrier to interconversion but are not inconsistent with a switchable Class II/III system. Although Dunbar and co-workers consider a statistical mixture of high-spin Co(II) and low-spin Co(III) to be a more likely scenario as compared to charge delocalization, due to the absence of an orbital pathway between the Co ions, 49 spin densities in Figure 2 indicate spin polarization on the cyano ligands. This may provide a pathway for Co \rightarrow Co MMCT that is mediated by Fe.

Attempts to optimize the geometry of the S = 7/2 state with the configuration $(\text{Co}^{2+})_2(\text{Co}^{3+})(\text{Fe}^{2+})(\text{Fe}^{3+})$ were unsuccessful, inevitably collapsing to $(\text{Co}^{2+})_3(\text{Fe}^{3+})_2$ with two

high-spin Co(II) ions, one low-spin Co(II), and two Fe(III) ions with opposite spins. This form, which is observed by Dunbar and co-workers when the material is dried at high temperature under inert conditions, ^{48,49} appears to be much lower in energy. Specifically, a S=9/2 state corresponding to $(\mathrm{Co^{2+}})_3(\mathrm{Fe^{3+}})_2$ with all-parallel unpaired spins is 10 kcal/mol more stable than the S=3/2 state at the optimized geometry of the latter, and 132 kcal/mol more stable at its own optimized geometry.

Temperature-Dependent XPS

Figure 3 shows the XPS spectra of Co₃Fe₂ at temperatures ranging from 150 to 375 K. Fitting these spectra provides the oxidation state distribution of the two Fe and three Co metal centers as a function of temperature. Figure 3A shows the Fe and Co 2p regions for three representative temperatures. At 150 K, the Fe edge shows 88.1% Fe²⁺ and 11.9% Fe³⁺, while the Co edge shows 44.6% Co²⁺ and 55.4% Co³⁺. By increasing the temperature to 298 K, the $\mathrm{Fe^{3+}}$ contribution increases to 35.6% as the Fe oxidizes, and the $\mathrm{Co^{2+}}$ contribution increases to 53.1% as the Co reduces. By 375 K the contribution of oxidized $\mathrm{Fe^{3+}}$ has increased to 49.7%, and the contribution of reduced Co²⁺ has increased to 60.6%. Quantification of Fe and Co oxidation state ratios for the complete temperature series is shown in Figure 3B. These data are consistent with a near unity electron transfer from Fe to Co. From these results, it is clear that a one electron MMCT occurs between the Fe and Co sites as a function of temperature, where a near unity loss of charge on one metal is balanced by a corresponding gain of charge on the other metal. Assuming a weakly coupled system (Robin Day Class I), this reflects a temperature-driven switch from a primarily $(\mathrm{Co^{2+}})(\mathrm{Co^{3+}})_2(\mathrm{Fe^{2+}})_2$ state to a primarily $(\mathrm{Co^{2+}})_2(\mathrm{Co^{3+}})(\mathrm{Fe^{2+}})$ state. However, assuming a strongly coupled system (Class II/III), this same MMCT could be equally well-described as a switch from $(\text{Co}^{2.7+})_3(\text{Fe}^{2+})_2$ to a $(\text{Co}^{2.3+})_2(\text{Fe}^{2+})(\text{Fe}^{3+})$, where strong Fe-CN-Co coupling makes individual Co centers indistinguishable.

In either case, it is possible to define the effective electron balance during this MMCT process as

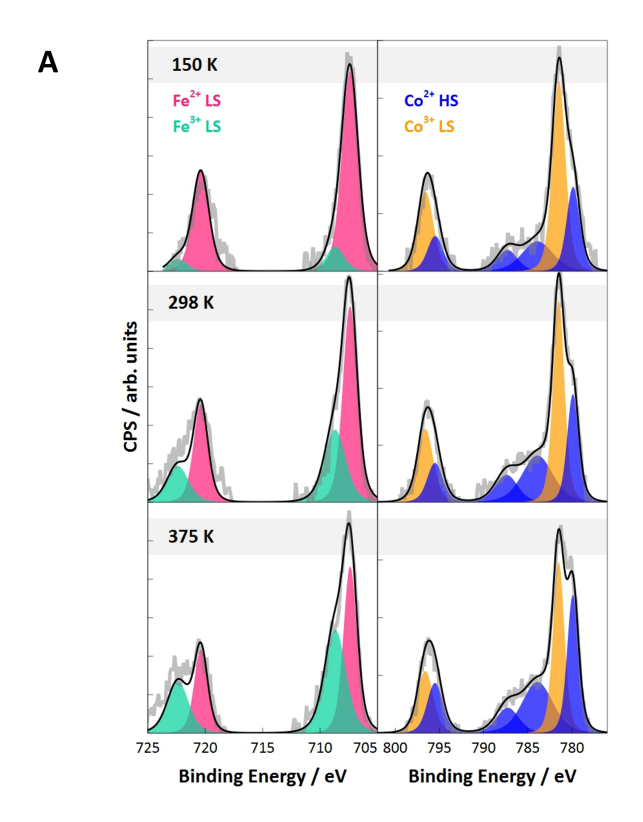
electron balance =
$$(2A_{\text{Fe}^{2+}} + 3A_{\text{Co}^{2+}})/3$$
.

where A is the area for the Fe and Co centers extracted from the XPS fits and weighted with the quantity of metal centers to reach a normalized value. As expected, the electron balance remains close to unity for all XPS spectra measured between 150 and 375 K consistent with a temperature-induced MMCT process. This is shown in Figure 4.

Chemical Environment-Dependent XPS

While temperature-dependent XPS spectra are consistent with a MMCT switching mechanism, Figure 5 shows the effect of chemical environment-induced state switching measured with NAP-XPS for the Fe and Co 2p spectra under ultrahigh vacuum (UHV) and 2 mbar water vapor held at room temperature. In this series, the same sample was cycled from UHV to water vapor and pumped again to UHV to evaluate the reversibility of the switching process induced by interaction with water vapor. When initially exposed to a UHV environment, the Fe 2p XPS spectrum appears as expected with both Fe²⁺ and Fe³⁺ present. The Co 2p spectrum shows a distribution of Co²⁺ and Co³⁺ character in approximately a 2:1 ratio. Introducing water to the system results in a reduction of Fe³⁺ to Fe²⁺. Surprisingly, the Co 2p spectrum shows slight oxidation of the Co, but

this change is less than expected for a unity electron transfer from Co to Fe. When the water vapor is pumped out, and UHV conditions are reestablished, the process reverses. This is observed in the Fe 2p spectrum as the single Fe²⁺ splits back into a near-equal contribution of Fe^{2/3+}. Again the Co 2p spectrum also reverses, but the change is less than expected for a full electron transfer between Fe and Co. These



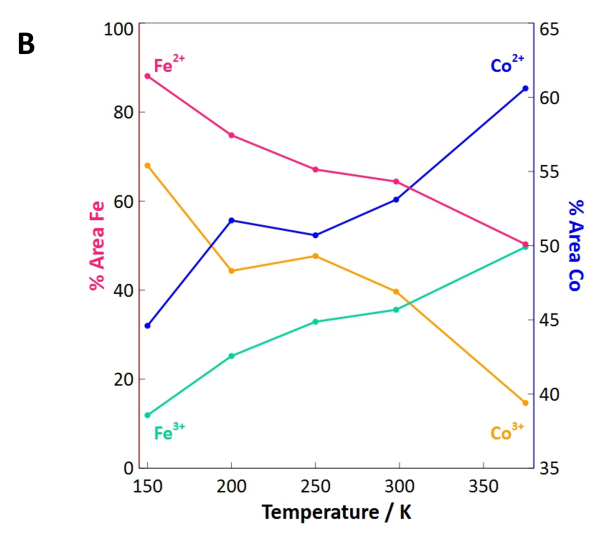


Figure 3. (A) NAP-XPS results at 150, 298, and 375 K of the Fe 2p (left) and Co 2p (right) edges. Total background-subtracted counts are shown as the gray solid line. The total fit is shown as the black solid line. Individual components are highlighted in pink (Fe²⁺), green (Fe³⁺), blue (Co²⁺), and orange (Co³⁺). (B) Fe and Co % area from NAP-XPS spectral fits as a function of temperature. Each solid line represents a different oxidation state, where Fe²⁺ is in pink, Fe³⁺ is in green, Co²⁺ is in blue, and Co³⁺ is in orange.

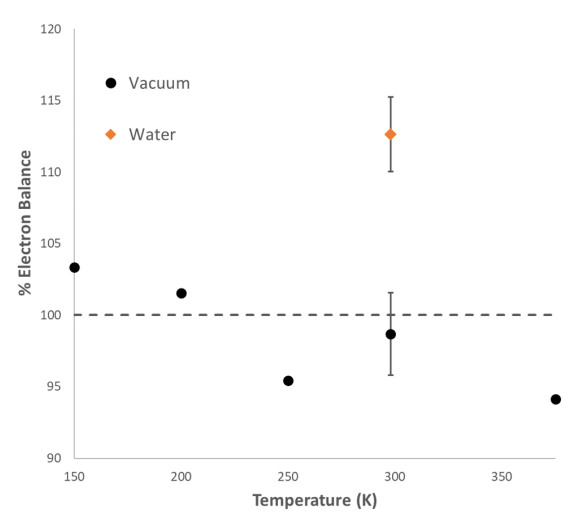
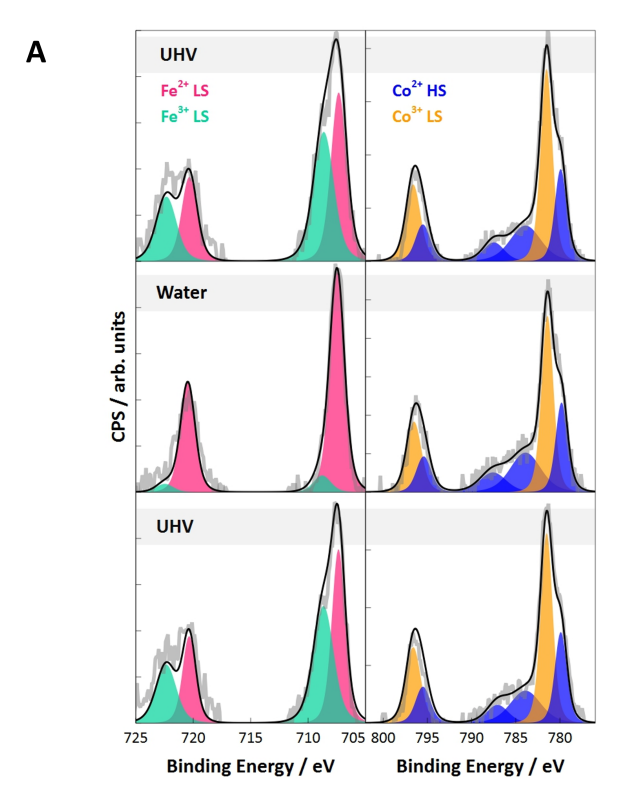


Figure 4. % electron balance calculated for charge transfers at each temperature under vacuum (black circles) and with water exposure at room temperature (orange diamond). A dashed line at 100% is shown for reference to a unity MMCT.

findings highlight an important difference between temperature and chemical environment-induced switching in this complex. Comparing the electron balance for temperature-dependent spectra with multiple spectra measured in UHV and 2 mbar water at 298 K show that upon exposure to water vapor, the electron balance exceeds unity with statistical significance as shown in Figure 4.

We now consider multiple potential mechanisms to explain this surprising behavior. First, it is possible that exposure of the sample surface to X-ray radiation during XPS measurements can induce beam damage that mistakenly appears as a change in the chemical state of the material. The first indication that this is not the case is the reversibility of the chemical state as the sample condition is cycled between UHV and water vapor. As the 2 mbar water vapor is removed from the sample chamber and the environment is returned to UHV conditions, the sample consistently showed a reversal back to its original state. This indicates that permanent sample damage by X-ray radiation is not occurring. To further exclude the possibility of beam-induced sample damage as a function of X-ray exposure, the following experiment was performed. Sitting at a single point on the sample, we collected 4 replicate XPS scans under a fixed condition. Following these four scans the pressure of water vapor was increased from UHV to 0.5 mbar and then to 2.0 mbar. Four replicate scans were collected under each condition. Results of this experiment are shown in Figure S4 in the Supporting Information. If reduction of Fe were the result of X-ray exposure, we would expect to observe a steady decrease of Fe³⁺ accompanied by a steady growth of Fe²⁺ as a function of X-ray exposure or scan number. However, instead we observe that the Fe 2p spectrum remains unchanged with scan number until the water pressure is increased at which point a step-wise reduction of Fe is observed. These observations indicate that the Fe reduction is a direct result of water exposure and not beam damage due to X-ray radiation.

A second possibility that could explain the reduction of Fe observed in Figure 5 is photoionization of the gas phase solvent by the X-ray source followed by electron attachment to Fe. To investigate this possibility, another solvent with a much higher photoionization cross section compared to wa-



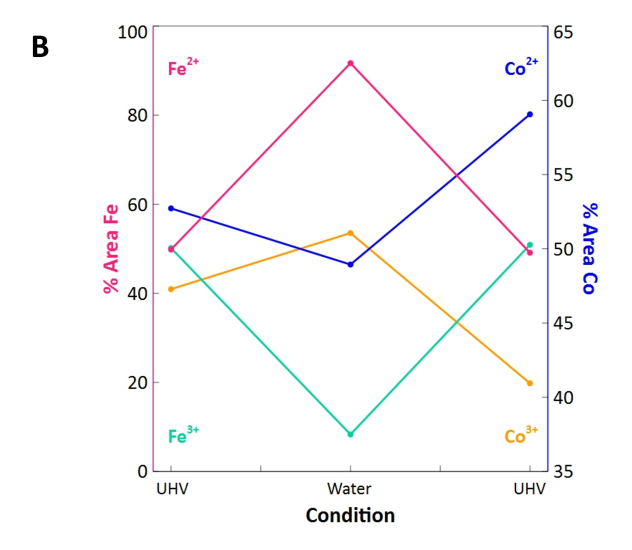


Figure 5. (A) NAP-XPS results at UHV, water, and post-exposure UHV of the Fe 2p (left) and Co 2p (right) edges. Total background-subtracted counts are shown as the gray solid line. The total fit is shown as the black solid line. Individual components are highlighted in pink (Fe²⁺), green (Fe³⁺), blue (Co²⁺), and orange (Co³⁺). (B) Fe and Co % area from NAP-XPS spectral fits as a function of chemical environment. Each solid line represents a different oxidation state, where Fe²⁺ is in pink, Fe³⁺ is in green, Co²⁺ is in blue, and Co³⁺ is in orange.

ter, carbon tetrachloride (CCl₄), was introduced to the sample chamber for NAP-XPS measurements. The results from this measurement are shown in Figure S5 of the Supporting Information. In summary, there is a negligible change in either the Fe or Co oxidation states as the sample is transitioned from UHV conditions to exposure to CCl₄ vapor. Fitting these spectra show that the Fe reduction between

UHV and CCl_4 exposure is 11.3%, compared to 83.4% in the case of water. This confirms that X-ray ionization of the background solvent cannot explain the reduction of Fe^{3+} to Fe^{2+} in the presence of water vapor.

Third, having eliminated potential effects of X-ray exposure, we evaluate the possibility of charge transfer between metal center and a phenanthroline ligand molecule in the Co₃Fe₂ complex. Considering that the aromatic phenanthroline groups may be redox active, it is possible that the electron transfer responsible for Fe reduction comes from a non-innocent phenanthroline ligand. If this is the case, we may expect to observe a shift in the N 1s XPS spectrum corresponding to oxidation of a phenanthroline ligand. The N 1s spectrum of this complex shows two peaks, which can be assigned to the phenanthroline ligands (399 eV) and the cyanide ligands (397 eV), respectively. Figure S6 in the Supporting Information shows the N 1s spectra as a function of temperature and as a function of chemical environment. In both cases, we observe minimal shift of the N peaks suggesting that redox activity of the ligands is not responsible for the reduction of Fe observed in Figure 5. To further support this conclusion, we note that the aromatic phenananthroline ligands coordinate only to the equatorial Co centers but that we observe redox cycling only of the axial Fe centers upon exposure to water vapor. While we cannot completely eliminate some redox activity by the phenanthroline ligands, below we consider a fourth possible mechanism involving a change in the electronic coupling between metal centers in the presence and absence of water vapor.

The fourth mechanism we consider to explain the observed results is that H-bonding of polar water molecules to the terminal cyanide ligands in the Co₃Fe₂ complex changes the electronic superexchange coupling between Fe and Co. As shown above in Figure 1, this can be described as a change in the Robin-Day classification from a strongly coupled complex (Class II/III) to moderately or weakly coupled system (Class I). In a strongly coupled system, electron density would be shared between an axial Fe center and its three neighboring equatorial Co centers. At the limit where electron hopping between Fe and Co is facile, then the individual Co centers would become indistinguishable. In the presence of water vapor, H-bonding to the terminal cyanide ligands will have an electron withdrawing effect, which would make the Fe³⁺ centers easier to reduce, resulting in electron transfer from the delocalized system to reduce Fe^{3+} to Fe^{2+} . Because the Fe²⁺-CN bond length is greater than the Fe³⁺-CN bond, 1.97 Å vs 1.94 Å in ferro- vs ferricyanide, ⁶¹ this would also reduce the superexchange coupling resulting in a change from a strongly coupled Class II/III system to a weakly coupled Class I system. In this scenario, we would expect to observe a near unity change in the oxidation state of the axial Fe³⁺ center to Fe²⁺, while the decoupling of the three equatorial Co centers with the axial Fe would result in a switch from $(\text{Co}^{2.3+})_3$ in the strongly coupled state to $(\mathrm{Co}^{2+})(\mathrm{Co}^{3+})_2$ in the weakly coupled state.

This change, supported by the DFT calculations described above, would be difficult to discern by XPS fitting of the Co 2p spectrum, which simplistically assumes a linear combination of distinct oxidation states and is insufficient to describe a switch from a strongly coupled Class II/III to a weakly coupled Class I system. If correct, this mechanism would further imply a change in both the symmetry and the local dipole moment along the equatorial axis of this molecule, whereas in the strongly coupled state all three Co centers are

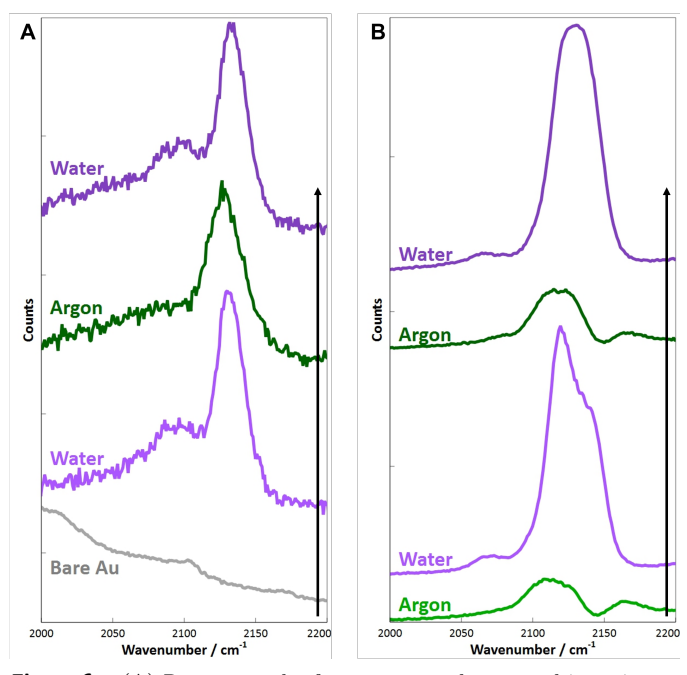


Figure 6. (A) Raman results from one sample exposed in series to water followed by argon and repeated water conditions. Bare Au measurement from the substrate of the sample is shown below in gray, which was subtracted from the other conditions to give absolute sample signal. (B) SFG-VS results from one sample exposed in series to argon and water followed by repeated argon and water conditions.

equivalent such that no dipole moment exists in the equatorial plane, while in the weakly coupled system, discrete Co oxidation states would create a significant in-plane dipole moment. Below, we utilize nonlinear, second order sum frequency generation vibrational spectroscopy of the cyanide bands to provide evidence in support of this mechanism.

Chemical Environment-Dependent Vibrational Spectroscopy

For vibrational spectroscopy measurements, the sample was placed in a small enclosed cell filled with either inert argon gas (simulates the anhydrous UHV conditions in Figure 5) or water vapor. While actively purging the cell with either argon or water, a Raman microscope collected vibrational spectra to probe the effect of chemical environment using the vibrational resonances of the cyanide ligands (2000–2200 cm⁻¹) as a reporter. Figure 6A shows that cycling between argon and water results in reversible spectral changes, suggesting that the Raman spectra are sensitive to the same chemically-induced switching process as observed above by NAP-XPS measurements. This is not surprising given the important role of the cyanide ligands to control the strength of superexchange coupling between Fe and Co centers.

In the initial spectrum acquired in water vapor (purple, bottom), we observe two features at 2094 and 2133 cm⁻¹, consistent with the nitrile stretch for terminal and bridging cyanide ligands, respectively. These assignments have been well-reported for Fe- and Co-coordinated cyanide ligands, where terminal Fe-CN ligands display vibrational resonances between 2060-2110 cm⁻¹ and bridging Fe-CN-Co ligands display resonances from 2090 to greater than 2170 cm⁻¹. ⁶²⁻⁶⁴ Within this range of frequencies, small shifts may reflect changes in the oxidation state of the coordinated metal center, where in general reduction of the metal leads to a spec-

tral red shift while oxidation of the metal leads to a blue shift. These shifts tend to be more sensitive to changes in the Co rather than Fe oxidation state due to the greater σ bonding character of the lower energy N lone pair mixing with the Co in the Co–N bond. 64

Under initial water conditions, the bridging cyanide peak is centered at $2133~\rm cm^{-1}$ while the terminal cyanide peak is centered at $2094~\rm cm^{-1}$. As argon is flowed through the cell and water vapor is removed, the bridging cyanide peak red shifts slightly to 2126 cm⁻¹ and the terminal cyanide peak broadens (green, middle). Close inspection of the spectrum reveals that the primary peak at 2126 cm⁻¹ broadens relative to the spectrum in water with a tail on the low frequency side. Because the spectrum in argon shows only one primary peak with a larger width and a tail at low frequency, we hypothesize that the terminal cyanide stretches, which appeared as a single peak in water having two divalent Fe^{2+} centers, splits in argon where the complex has both an Fe²⁺ and Fe³⁺ center on on each apex (see Figure 5). In this state, the blue-shifted terminal cyanide stretches associated with the Fe^{3+} center overlap with the red-shifted bridging cyanide stretches associated with the reduced Co centers. Importantly, these spectral changes are reversible and reintroduction of water results in nearly exact recovery of the original spectrum (purple, top). These observations are qualitatively consistent with the spectral changes anticipated for a MMCT transition between Fe and Co in the presence and absence of water as a H-bonding solvent.

While the Raman measurements support the assignment of a MMCT driven by a change in chemical environment, it does not specifically resolve the degree of electronic (de)localization or differentiate between the strongly coupled (Robin-Day Class II/III) and weakly coupled (Robin-Day Class I) pictures. To investigate this question further, we compare the environment-dependent Raman spectra with SFG-VS spectra obtained under identical conditions of argon and water vapor (see Figure 6B). This measurement is insightful because as a second order, nonlinear process, SFG is sensitive to the centrosymmetry of the system, and vibrational resonances become dipole-forbidden in a locally centrosymmetric environment. This indicates that in a strongly coupled state of the molecule where the oxidation states of the three Co centers are identical (see Figure 1B), there should be little or no signal from the bridging cyanide ligands due to the local symmetry of these ligands in the equatorial plane of the molecule.

We note that broken inversion symmetry can also result from non-identical Fe centers on the axial positions of the complex. However, as discussed above, the cyanide stretch of bridging ligands are relatively insensitive to the Fe oxidation state compared to Co oxidation state due to greater σ bonding character of the lower energy N lone pair mixing with the Co. Consequently, we expect the intensity of the bridging Fe–CN–Co stretches to report most sensitively on the molecular symmetry of the equatorial plane as determined by the oxidation states of the Co centers. In this way, SFG intensity becomes a probe of electronic superexchange coupling, where distinct Co oxidation states in a weakly coupled system will show higher signal intensity compared to identical Co oxidation states in a strongly coupled system, which will show little to no SFG intensity.

Figure 6B shows the SFG-VS measurement of a sample cycled between argon and water conditions. The peak shifts between water and argon environments are the same as the

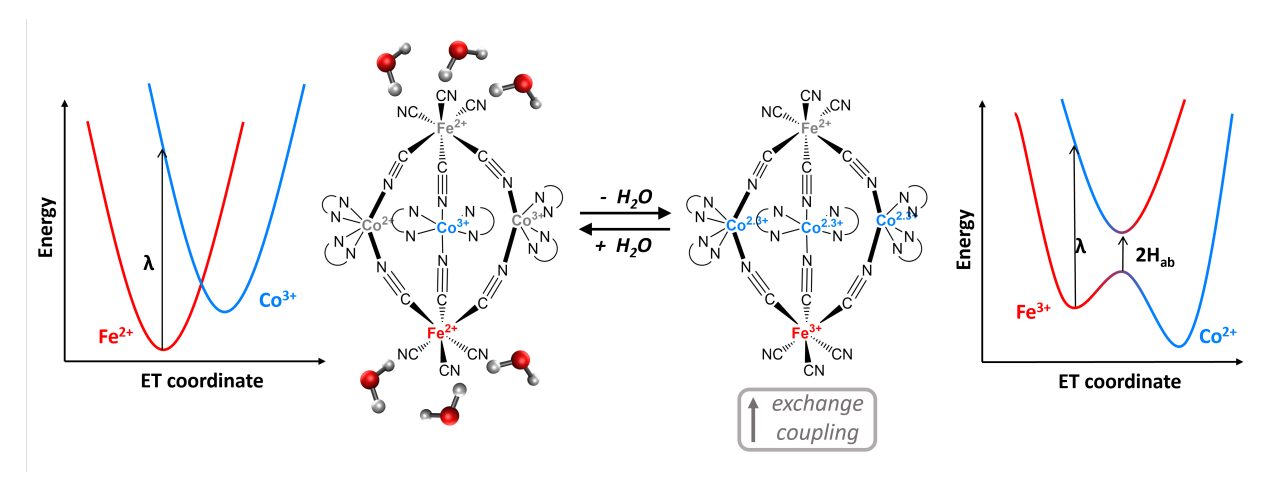


Figure 7. Mechanism for complex changes under ambient and vacuum/argon conditions. There is a MMCT event coupled with a change in the electronic (de)localization, depicted with distinct versus equivalent oxidation states. On the left, the molecule has H-bonding water molecules at the terminal cyanide ligands, reducing the coupling and resulting in a Class I system. On the right, exchange coupling increases upon dehydration and the system behaves as a Class II/III molecule with indistinguishable Co oxidation states and the absence of an equatorial dipole.

changes observed in the Raman measurements. Exposed to initial argon conditions, the bridging cyanide peak is centered at 2114 cm⁻¹ with a broad FWHM indicating the terminal cyanide peak is spectrally overlapping with the bridging feature. When water is introduced to the sample, the bridging cyanide peak shifts to a central position of 2129 cm⁻¹ while the terminal cyanide peak is isolated at 2069 cm⁻¹. With repeated exposure to argon and water conditions, these features shift reversibly. While the absolute positions and magnitude of the shift is not identical between Figures 6A and 6B, the qualitative trends match.

Beyond the peak shifts observed in Raman, the SFG results in Figure 6B also display a significant intensity difference depending on the sample environment. In the presence of water, the signal intensity shows approximately a fourfold increase relative to argon. Because SFG is sensitive to the molecular symmetry through the second order polarizability, this observation indicates that the dipole of the molecule changes in the presence or absence of water vapor.

At first, it is surprising that the intensity increases in water and decreases in argon because NAP-XPS measurements show that in water, both Fe centers are in the 2+ oxidation state, while in UHV or argon, the two Fe centers are in different, 2+ and 3+ oxidation states. This would suggest that molecular symmetry should increase in water, leading to a loss of SFG signal. Instead we see a significant signal enhancement in the presence of water. However, it is important to note that this intensity increase occurs in the bridging, rather than the terminal cyanide stretches. This strongly suggests that the spectrum is more sensitive to change in the Co charge states compared to Fe, as expected.

Considering how water vapor can change the charge distribution of the equatorial Co centers, so as to decrease the molecular symmetry and lead to enhanced SFG signal, we propose the following explanation. In a Robin-Day Class II/III system, where electron exchange between Fe and Co is facile, the molecule cannot support distinct oxidation states between Co centers as each is rapidly exchanging electrons with a common Fe center faster than the time scale of a vibrational resonance. In such a scenario, the SFG experiment observes a system where charge is evenly distributed among the three Co centers, leading to a loss of dipole moment in

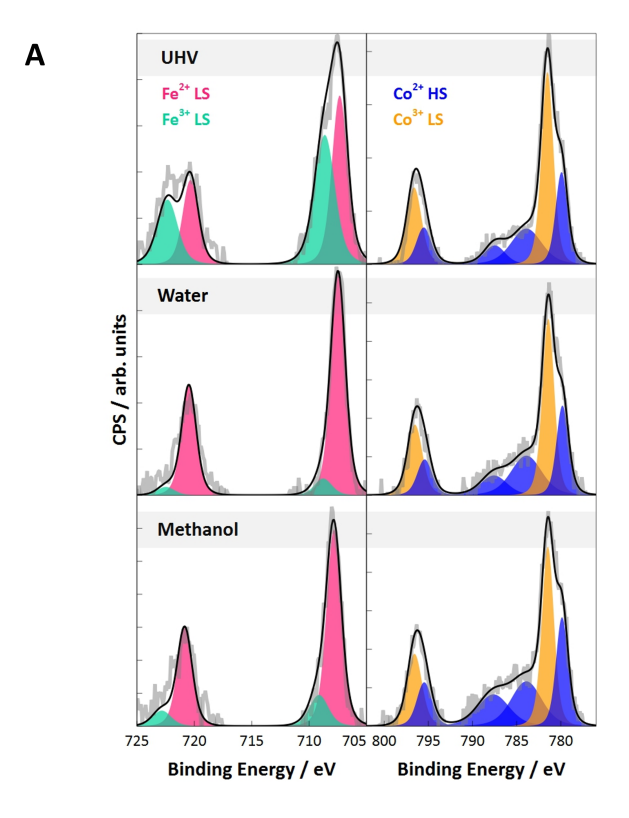
the equatorial plane of the molecule. Ignoring differences in the oxidation states of the terminal Fe centers, which minimally influence the cyanide stretching frequency, this state of the molecule would render each of the six cyanide ligands degenerate, leading to a high degree of local symmetry. This describes the strongly coupled state of the molecule observed in argon, showing weak SFG intensity of the highly symmetric, six-fold degenerate bridging cyanide stretches.

In contrast, water H-bonds to the terminal cyanide ligands shifts charge density to the terminal Fe atoms, leading to reduction of Fe³⁺ to Fe²⁺ by NAP-XPS (see Figure 5). It is known that a change in Fe oxidation state results in an increase of the Fe-CN bond, 65 leading to a reduction in the superexchange coupling. This reduction in the exchange coupling in the presence of water results in Co centers with discrete oxidation states, which would break the degeneracy of the six bridging cyanide ligands, leading to the formation of an in-plane dipole moment and the observed significant increase in SFG intensity. This mechanism is depicted schematically in Figure 7, which is also consistent with NAP-XPS measurements, which show that the overall charge balance on the Co centers changes between UHV and water vapor (see Figure 4), indicating a change in the charge (de)localization of the system depending on the chemical environment.

Lastly, we confirm that both the changes observed by NAP-XPS as well as SFG are sensitive to the H-bonding ability of the gas environment. Figure 8A shows the NAP-XPS spectra and Figure 8B shows the SFG spectra of the $\mathrm{Co_3Fe_2}$ complex in UHV or argon, water, and methanol vapor. We observe that the changes in Fe oxidation state from 3+ to 2+ observed by NAP-XPS is correlated with the intensity of the bridging cyanide ligands observed by SFG and appears to track with the H-bonding capacity of the chemical environment. These features steadily increase from inert environment (UHV or argon) to methanol to water.

Conclusion

This study compares the effects of temperature and gas environment on the chemical states of a bistable $\mathrm{Co_3Fe_2}$ complex. Using NAP-XPS as a probe of element specific oxidation states on Co and Fe centers provides a detailed pic-



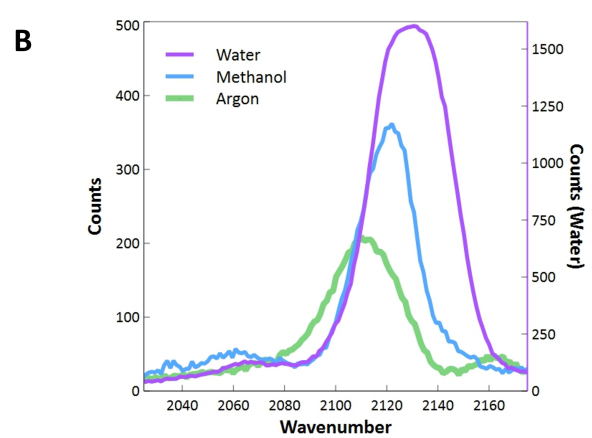


Figure 8. (A) NAP-XPS results under UHV, water, and methanol conditions for the Fe 2p (left) and Co 2p (right) edges. Total background-subtracted counts are shown as the gray solid line. The total fit is shown as the black solid line. Individual components are highlighted in pink (Fe²⁺), green (Fe³⁺), blue (Co²⁺), and orange (Co³⁺).(B) SFG-VS results from water, methanol, and argon conditions overlaid. The methanol and argon are plotted with absolute counts on the left axis while water is plotted with absolute counts on the right axis for scaling visual purposes.

ture of environment-induced MMCT transitions in this complex. Temperature-dependent NAP-XPS show a MMCT from Fe to Co as the temperature is increased from 150 to 375 K. However, NAP-XPS results show that the transition observed when cycling between UHV and water vapor cannot be simply explained as a MMCT transition. Complementary measurements by Raman and SFG-VS reveal that in addition to a chemically-induced MMCT, H-bonding of the $\rm Co_3Fe_2$ complex with water also modulates the strength of superexchange coupling resulting in a switch from a de-

localized to a localized electronic state, involving a corresponding change in the local symmetry and dipole moment of the complex. Specifically, the introduction of H-bonding solvents decreases the strength of superexchange coupling of the Fe–CN–Co system, resulting in a change from a delocalized electronic configuration (Robin-Day Class II/III) to a localized electronic configuration (Class I) that supports discrete Co center oxidation states, which reduces the molecular symmetry. This change in Robin-Day classification as a function of chemical environment results in reversible switching of the dipole moment, drawing an analogy to molecular multiferroics, and these results illustrate the important role of chemical environment and solvation on the underlying charge and spin transitions in this and related complexes.

Supporting Information

The Supporting Information is available free of charge on the ACS Publications website. Sample preparation (materials, [Co(tmphen)₂]₃[Fe(CN)₆]₂ (Co₃Fe₂), Co₃Fe₂ characterization, Co₃Fe₂ solution, solution drop-casting), XPS fitting parameters, NAP-XPS Controls (conditional exposure, X-ray exposure, Solvent photoionization, N 1s solvent exposure), SFG controls (clean substrate baseline, time delay interference, sample pseudo-homogeneity), single-crystal X-ray structure, DFT-optimized structures.

Notes

The authors declare the following competing financial interest(s): J.M.H. serves on the board of directors of Q-Chem Inc.

Acknowledgements

This work was primarily supported by Chemical Sciences, Geosciences and Biosciences Division, Office of Basic Energy Sciences, Office of Science, U.S. Department of Energy under DOE Grant No. DE-SC0020977. Synthesis and characterization of the compound was supported by Chemical Sciences, Geosciences and Biosciences Division, Office of Basic Energy Sciences, Office of Science, U.S. Department of Energy under DOE Grant No. DE-SC0020243. DFT calculations were supported by the National Science Foundation under NSF Grant No. CHE-1955282. XPS and NAP-XPS was performed at The Ohio State University Surface Analysis Laboratory. X-ray crystallography was performed at The Ohio State University X-ray Crystallography Laboratory. We thank Dr. Yehia Khalifa and Melissa Marx for assistance with NAP-XPS measurements, Dr. Curtis Moore for assistance with X-ray crystallography measurements, and Prof. Zachary Schultz and Dr. Chelsea Zoltowski for assistance with Raman measurements.

References

- (1) Wasielewski, M. R.; Forbes, M. D.; Frank, N. L.; Kowalski, K.; Scholes, G. D.; Yuen-Zhou, J.; Baldo, M. A.; Freedman, D. E.; Goldsmith, R. H.; Goodson III, T. et al. Exploiting chemistry and molecular systems for quantum information science. *Nature Reviews Chemistry* 2020, 4, 490–504.
- (2) Gaita-Ariño, A.; Luis, F.; Hill, S.; Coronado, E. Molecular spins for quantum computation. *Nature chemistry* 2019, 11, 301– 309.
- (3) Stajic, J. The future of quantum information processing. 2013.
 (4) Ardavan, A.; Rival, O.; Morton, J. J.; Blundell, S. J.; Tyryshkin, A. M.; Timco, G. A.; Winpenny, R. E. Will spinrelaxation times in molecular magnets permit quantum information processing? Physical review letters 2007, 98, 057201.
- (5) Hamlin, J. J.; Zhou, B. B. Extreme diamond-based quantum sensors. Science 2019, 366, 1312–1313.

- (6) Carmeli, I.: Kumar, K. S.: Heifler, O.: Carmeli, C.: Naaman, R. Spin selectivity in electron transfer in photosystem I. Angewandte Chemie International Edition 2014, 53, 8953-8958.
- Mai, S.; González, L. Molecular photochemistry: recent developments in theory. Angewandte Chemie International Edition
- 2020, 59, 16832–16846.

 Lambert, N.; Chen, Y.-N.; Cheng, Y.-C.; Li, C.-M.; Chen, G.-Y.; Nori, F. Quantum biology. Nature Physics 2013, 9, 10–18.
 Pan, L.; Ai, M.; Huang, C.; Yin, L.; Liu, X.; Zhang, R.; Wang, S.; Jiang, Z.; Zhang, X.; Zou, J.-J. et al. Manipulating spin polarization of titanium dioxide for efficient photocatalysis.

 Nature communications 2020, 11, 418.

 (10) Ferlay, S.; Mallah, T.; Ouahes, R.; Veillet, P.; Verdaguer, M.
- A room-temperature organometallic magnet based on Prussian blue. Nature 1995, 378, 701-703.
- Entley, W. R.; Girolami, G. S. High-temperature molecular magnets based on cyanovanadate building blocks: spontaneous magnetization at 230 K. Science 1995, 268, 397–400.
- (12) Holmes, S. M.; Girolami, G. S. Sol-Gel Synthesis of KV^{II} $\rm [Cr^{III}(CN)_6]\cdot 2H_2O:$ A Crystalline Molecule-Based Magnet with a Magnetic Ordering Temperature above 100 °C. Journal of the American Chemical Society 1999, 121, 5593-5594.
- (13) Sato, O.; Iyoda, T.; Fujishima, A.; Hashimoto, K. Photoinduced magnetization of a cobalt-iron cyanide. Science 1996, 272, 704-
- (14) Beauvais, L. G.; Long, J. R. Co3 [Co (CN) 5] 2: A microporous magnet with an ordering temperature of 38 K. Journal of the American Chemical Society 2002, 124, 12096–12097.
- (15) Berlinguette, C. P.; Vaughn, D.; Cañada-Vilalta, C.; Galán-Mascarós, J. R.; Dunbar, K. R. A Trigonal-Bipyramidal Cyanide Cluster with Single-Molecule-Magnet Behavior: Synthesis, Structure, and Magnetic Properties of {[MnII (tmphen) 2] 3 [MnIII (CN) 6] 2}. Angewandte Chemie International Edition **2003**, 42, 1523–1526.
- Shatruk, M.; Chambers, K. E.; Prosvirin, A. V.; Dunbar, K. R. Systematic investigation of trigonal-bipyramidal cyanide-bridged clusters of the first-row transition metals. *Inorganic chemistry* **2007**, *46*, 5155–5165.
- (17) Shatruk, M.; Dragulescu-Andrasi, A.; Chambers, K. E.; Stoian, S. A.; Bominaar, E. L.; Achim, C.; Dunbar, K. R. Properties of Prussian blue materials manifested in molecular complexes: observation of cyanide linkage isomerism and spin-
- complexes: observation of cyanide linkage isomerism and spincrossover behavior in pentanuclear cyanide clusters. Journal of the American Chemical Society 2007, 129, 6104-6116.
 (18) Berlinguette, C. P.; Dragulescu-Andrasi, A.; Sieber, A.; Galán-Mascarós, J. R.; Güdel, H.-U.; Achim, C.; Dunbar, K. R. A charge-transfer-induced spin transition in the discrete cyanide-bridged complex {[Co (tmphen) 2] 3 [Fe (CN) 6] 2}. Journal of the American Chemical Society 2004, 126, 6222-6223.
 (19) Shimamoto, N.; Ohkoshi, S.-i.; Sato, O.; Hashimoto, K. Control of characteristics for induced spin transition temperature on the control of characteristics for induced spin transition temperature.
- trol of charge-transfer-induced spin transition temperature on cobalt- iron Prussian blue analogues. Inorganic chemistry **2002**, *41*, 678–684.
- (20) Roman, M. A.; Reu, O. S.; Klokishner, S. I. Charge-transfer-induced spin transitions in crystals containing cyanide-bridged co-fe clusters: role of intra-and intercluster interactions. The Journal of Physical Chemistry A 2012, 116, 9534-9544.
- Zimara, J.; Stevens, H.; Oswald, R.; Demeshko, S.; Dechert, S.; Mata, R. A.; Meyer, F.; Schwarzer, D. Time-Resolved Spectroscopy of Photoinduced Electron Transfer in Dinuclear and Tetranuclear Fe/Co Prussian Blue Analogues. *Inorganic Chemistry* **2020**, *60*, 449–459. Schnaubelt, L.; Petzold, H.; Dmitrieva, E.; Rosenkranz, M.;
- Lang, H. A solvent-and temperature-dependent intramolecular equilibrium of diamagnetic and paramagnetic states in Co complexes bearing triaryl amines. Dalton Transactions 2018, 47, 13180–13189.
- Nadurata, V. L.; Boskovic, C. Switching metal complexes via intramolecular electron transfer: connections with solvatochromism. Inorganic Chemistry Frontiers 2021, 8, 1840-
- Funck, K. E.; Prosvirin, A. V.; Mathonière, C.; Clérac, R.; Dunbar, K. R. Light-induced excited spin state trapping and charge transfer in trigonal bipyramidal cyanide-bridged complexes. Inorganic chemistry **2011**, 50, 2782–2789.
- (25) Létard, J.-F. Photomagnetism of iron (II) spin crossover complexes—the T (LIESST) approach. Journal of Materials Chemistry 2006, 16, 2550–2559.
 Bleuzen, A.; Marvaud, V.; Mathoniere, C.; Sieklucka, B.; Verda-
- guer, M. Photomagnetism in clusters and extended moleculebased magnets. Inorganic chemistry 2009, 48, 3453-3466.
- Manriquez, J. M.; Yee, G. T.; McLean, R. S.; Epstein, A. J.; Miller, J. S. A room-temperature molecular/organic-based mag-
- net. Science 1991, 252, 1415–1417.
 Blundell, S. J.; Pratt, F. L. Organic and molecular magnets.
 Journal of Physics: Condensed Matter 2004, 16, R771.
- Miller, J. S.; Epstein, A. J. Organic and organometallic molecu- ${\tt lar\ magnetic\ materials--designer\ magnets.}\ Angewand te\ Chemie$ International Edition in English 1994, 33, 385–415.
- Miller, J. S. Magnetically ordered molecule-based materials. Chemical Society Reviews 2011, 40, 3266–3296.
- Ungur, L.; Chibotaru, L. F. Strategies toward high-temperature lanthanide-based single-molecule magnets. Inorganic Chem-

- istry 2016, 55, 10043-10056.
- Long, J.; Guari, Y.; Ferreira, R. A.; Carlos, L. D.; Larionova, J. Recent advances in luminescent lanthanide based Single-Molecule Magnets. Coordination Chemistry Reviews **2018**, 363, 57-70.
- (33) Ren, M.; Zheng, L.-M. Lanthanide-based single molecule magnets. Acta Chimica Sinica 2015, 73, 1091. Liu, J.-L.; Chen, Y.-C.; Tong, M.-L. Symmetry strategies for
- high performance lanthanide-based single-molecule magnets. Chemical Society Reviews 2018, 47, 2431-2453.
- (35) Benelli, C.; Gatteschi, D. Introduction to molecular magnetism: From transition metals to lanthanides; John Wiley & Sons, 2015.
- Parker, D.; Suturina, E. A.; Kuprov, I.; Chilton, N. F. How the ligand field in lanthanide coordination complexes determines magnetic susceptibility anisotropy, paramagnetic NMR shift, and relaxation behavior. Accounts of Chemical Research **2020**, *53*, 1520–1534.
- Gomez-Coca, S.; Cremades, E.; Aliaga-Alcalde, N.; Ruiz, E. Mononuclear single-molecule magnets: tailoring the magnetic anisotropy of first-row transition-metal complexes. Journal of the American Chemical Society 2013, 135, 7010–7018.
- Wang, J.-H.; Li, Z.-Y.; Yamashita, M.; Bu, X.-H. Recent progress on cyano-bridged transition-metal-based singlemolecule magnets and single-chain magnets. Coordination Chemistry Reviews 2021, 428, 213617.
- (39) Bar, A. K.; Pichon, C.; Sutter, J.-P. Magnetic anisotropy in twoto eight-coordinated transition-metal complexes: Recent developments in molecular magnetism. Coordination Chemistry Reviews 2016, 308, 346–380.
- (40) Dunbar, K. R.; Heintz, R. A., et al. Chemistry of transition metal cyanide compounds: Modern perspectives. Progress in inorganic chemistry 1997, 45, 283–392. (41) Shatruk, M.; Avendano, C.; Dunbar, K. R. Cyanide-bridged
- complexes of transition metals: A molecular magnetism per-
- spective. Progress in inorganic chemistry 2009, 56, 155–334. Meng, L.; Deng, Y.-F.; Zhang, Y.-Z. Anion-Dependent Electron Transfer in the Cyanide-Bridged [Fe2Co2] Capsules. Inorganic
- Transfer in the Cyanide-Bridged [Fe2Co2] Capsules. Inorganic Chemistry 2021, 60, 14330–14335.

 Han, M. J.; Ozaki, T.; Yu, J. Electronic structure, magnetic interactions, and the role of ligands in Mn n (n= 4, 12) single-molecule magnets. Physical Review B 2004, 70, 184421.

 Sharma, P.; Truhlar, D. G.; Gagliardi, L. Magnetic coupling in a tris-hydroxo-bridged chromium dimer occurs through ligand
- mediated superexchange in conjunction with through-space coupling. Journal of the American Chemical Society 2020, 142, 16644-16650.
- (45) Robin, M. B.; Day, P. Mixed valence chemistry—a survey and classification. Adv. Inorg. Chem. Radiochem. 1968, 10, 247-
- (46) Demadis, K. D.; Hartshorn, C. M.; Meyer, T. J. The localizedto-delocalized transition in mixed-valence chemistry. Chemical reviews 2001, 101, 2655–2686.
- (47) Parthey, M.; Kaupp, M. Quantum-chemical insights into mixedvalence systems: within and beyond the Robin–Day scheme. Chemical Society Reviews 2014, 43, 5067–5088.
- Funck, K. E.; Hilfiger, M. G.; Berlinguette, C. P.; Shatruk, M.; Wernsdorfer, W.; Dunbar, K. R. Trigonal-bipyramidal metal cyanide complexes: a versatile platform for the systematic assessment of the magnetic properties of Prussian blue materials. Inorganic chemistry **2009**, 48, 3438–3452.
- Berlinguette, C. P.; Dragulescu-Andrasi, A.; Sieber, A.; Güdel, H.-U.; Achim, C.; Dunbar, K. R. A charge-transferinduced spin transition in a discrete complex: the role of extrinsic factors in stabilizing three electronic isomeric forms of a cyanide-bridged Co/Fe cluster. Journal of the American Chemical Society 2005, 127, 6766-6779.
- Wallentine, S.; Bandaranayake, S.; Biswas, S.; Baker, L. R. Plasmon-resonant vibrational sum frequency generation of electrochemical interfaces: Direct observation of carbon dioxide electroreduction on gold. The Journal of Physical Chemistry
- A 2020, 124, 8057–8064.

 (51) Zhu, Q.; Wallentine, S. K.; Deng, G.-H.; Rebstock, J. A.; Baker, L. R. The solvation-induced Onsager reaction field rather than the double-layer field controls CO2 reduction on gold. JACS Au 2022, 2, 472-482.
- (52) Renz, M.; Theilacker, K.; Lambert, C.; Kaupp, M. A reliable quantum-chemical protocol for the characterization of organic mixed-valence compounds. Journal of the American Chemical Society 2009, 131, 16292–16302.
- (53) Grimme, S.; Antony, J.; Ehrlich, S.; Krieg, H. A consistent and accurate *ab initio* parameterization of density functional dispersion correction (DFT-D) for the 94 elements H–Pu. *Journal* of Chemical Physics 2010, 132, 154104:1-19.
- Neese, F. Prediction of molecular properties and molecular spectroscopy with density functional theory: From fundamental theory to exchange-coupling. Coordination Chemistry Reviews **2009**, *253*, 526–563.
- Epifanovsky, E.; Gilbert, A. T. B.; Feng, X.; Lee, J.; Mao, Y.; Mardirossian, N.; Pokhilko, P.; White, A. F.; Coons, M. P.; Dempwolff, A. L. et al. Software for the frontiers of quantum chemistry: An overview of developments in the Q-Chem 5 pack-
- age. Journal of Chemical Physics 2021, 155, 084801.
 (56) Szilagyi, R. K.; Winslow, M. A. On the accuracy of density func-

- tional theory for iron-sulfur clusters. Journal of Computational
- tional theory for iron-sulfur clusters. Journal of Computational Chemistry 2006, 27, 1385-1397.
 (57) Ren, F.; Liu, F. Impacts of polarizable continuum models on the SCF convergence and DFT delocalization error of large molecules. Journal of Chemical Physics 2022, 157, 184106.
 (58) Bowling, P. E.; Broderick, D. R.; Herbert, J. M. Fragment-based calculations of enzymatic thermochemistry require dielectics.
- tric boundary conditions. Journal of Physical Chemistry Letters **2023**, *14*, 3826–3834.
 (59) Lange, A. W.; Herbert, J. M. Polarizable continuum reaction-
- field solvation models affording smooth potential energy surfaces. Journal of Physical Chemistry Letters 2010, 1, 556–561.

 (60) Lange, A. W.; Herbert, J. M. A smooth, nonsingular, and
- faithful discretization scheme for polarizable continuum models: The switching/Gaussian approach. Journal of Chemical
- Physics 2010, 133, 244111.

 (61) Smith, D. A.; Heeg, M.; Heineman, W. R.; Elder, R. Direct determination of Fe-C bond lengths in iron (II) and iron (III) cyanide solutions using EXAFS spectroelectrochemistry. Journal of the American Chemical Society 1984, 106, 3053-3054.
- (62) Hester, R. E., et al. Resonance-Raman and infrared studies of cyanide-bridged dimetal complexes. Journal of the Chemical
- Society, Dalton Transactions 1981, 939–941. Nihei, M.; Sekine, Y.; Suganami, N.; Nakazawa, K.; Nakao, A.; Nakao, H.; Murakami, Y.; Oshio, H. Controlled intramolecular electron transfers in cyanide-bridged molecular squares by chemical modifications and external stimuli. Journal of the Ameri $can\ Chemical\ Society\ {\bf 2011},\ 133,\ 3592-3600.$
- can Chemical Society 2011, 133, 3392-3000.
 (64) Kettle, S. F.; Diana, E.; Boccaleri, E.; Stanghellini, P. L. The vibrational spectra of the cyanide ligand revisited. Bridging cyanides. Inorganic chemistry 2007, 46, 2409-2416.
 (65) Nihei, M.; Yanai, Y.; Hsu, I.-J.; Sekine, Y.; Oshio, H. A Hydrogen-Bonded Cyanide-Bridged [Co2Fe2] Square Complex Exhibition Three Standard Conference of Conference
- Exhibiting a Three-Step Spin Transition. Angewandte Chemie International Edition 2017, 56, 591–594.